Article

Comparative statistical analysis of pitting in Two 2205 duplex stainless steel variants

Check for updates
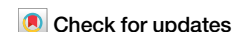
Guoyong Ran[1], Wenrui Tu[1], Haopeng Dong[2], Yiming Jiang[1], Jin Li[1,3], Kezhao Liu[2] & Yangting Sun [1] ✉

The inherent variability of pitting poses challenges in accurately evaluating the pitting resistance due to potential disparities in test results. This study compares the pitting resistance of two commercial 2205 duplex stainless steels. Counterintuitively, the variant with higher Pitting Resistance Equivalent Number, exhibits a lower Critical Pitting Temperature. Through the potentiostatic pulse test and potentiostatic polarization, this variant is observed to have a greater number of pitting initiation sites. Further investigation, using SEM inclusion statistics, reveals an increased presence of inclusions rich in calcium oxides as the underlying cause of this unexpected phenomenon.

The stable pitting process in stainless steel comprises distinct stages: nucleation, metastable growth, and steady-state propagation[1]. These stages are influenced by various factors. Consequently, pitting occurs randomly under specific conditions of solution medium, potential and temperature[2]. In the case of highly corrosion-resistant steels, this randomness may become more pronounced, thus complicating the evaluation of pitting behavior[3,4].

The pitting resistance of stainless steel is primarily controlled by alloying content. The Pitting Resistance Equivalent Number (PREN) is commonly used as a measure of pitting resistance[5–10]. In duplex stainless steel (DSS), the pitting resistance is influenced by the PREN of both austenite (γ) and ferrite (α) phases, and optimal performance is achieved when the austenite-ferrite ratio is close to 1:1[11,12]. However, it is essential to note that while PREN offers a direct, efficient, and preliminary assessment of pitting resistance, it is a simplistic and empirical parameter[5,6]. PREN does not take into account factors such as surface roughness[13], presence of heterogeneous particles[14–16] and the local variations[17,18] of the protection properties of the passive film. As a result, when comparing stainless steels with similar pitting resistance, reliance solely on PREN may lead to inaccurate conclusions.

The Critical Pitting Temperature (CPT) is often considered a more accurate parameter for characterizing pitting resistance. However, when comparing two samples with similar resistance, their respective CPT dispersion may significantly overshadow their differences[19–22]. Previous studies have indicated that the potentiodynamic CPT (Z-curve) provides a more reliable measure of pitting resistance than potentiostatic CPT[23]. Nevertheless, obtaining potentiodynamic CPT values necessitates extensive data accumulation, potentially leading to time-consuming efforts, and it only yields temperature values, which may hinder a comprehensive understanding of the process and mechanism of pitting. Consequently, evaluating high-performance stainless steels with similar pitting characteristics remains a significant challenge[19]. Moreover, the initiation process of pitting plays a crucial role in high performance stainless steel, thus further investigation into the initiation process is necessary.

The potentiostatic pulse test (PPT) is capable of inducing a considerable number of pits simultaneously, enabling more efficient statistical evaluation and mitigating the influence of pitting randomness[23]. More importantly, it can retain early information about pitting development through parameter control, thereby enabling convenient research into the initiation behavior of pitting[15,24,25].

In this study we undertake a comparative assessment of two types of 2205 DSS, which were provided by two different companies. These are designated as 2205-A and 2205-B, respectively. The specifications of both 2205-A and 2205-B are summarized in Table 1. The relative pitting resistance as suggested by PREN contradicts with that revealed by CPT. To reconcile this discrepancy, we conducted a series of PPT tests accompanied by corresponding morphological characterizations, allowing for an exhaustive statistical analysis. The results show that the discrepancy can be attributed to the disparity in the amount of calcium-containing complex oxide inclusions.

Results
Microstructure
The optical morphologies of 2205-A and 2205-B etched by Murakami solution are illustrated in Fig. 1. The brown regions represent the α phase, while the white regions represent the γ phase. In Fig. 1a, c, two phases of both hot-rolled specimens are elongated parallel to the rolling direction (RD).

[1]Department of Materials Science, State Key Laboratory of Molecular Engineering of Polymers, Fudan University, Shanghai 200433, PR China. [2]Institute of Materials, China Academy of Engineering Physics, Jiangyou 621700, PR China. [3]School of Materials Science and Engineering, State Key Lab of Marine Resource Utilization in South China Sea, Hainan University, Haikou 570228, PR China. ✉e-mail: sunyangting@fudan.edu.cn

Table 1 | Composition of two types of 2205 DSS

Materials	Cr	Ni	Mo	N	Mn	C	Si	S	P	Fe
2205-A	22.32	5.23	2.93	0.15	1.19	0.022	0.55	<0.001	0.025	Bal
2205-B	22.27	5.46	3.10	0.15	1.37	0.026	0.47	<0.001	0.023	Bal

Further examination at higher magnification reveals the absence of black carbides or any discernible third phase (Fig. 1b, d). The X-ray diffraction (XRD) pattern (Fig. 1e) also confirms that both types of 2205 DSS consist of α and γ phases.

ImageJ software is utilized to calculate the phase proportions of 2205-A and 2205-B, as shown in Table 2. The average elemental compositions of α and γ, which were determined through EDS at 10 different positions, were used for PREN calculation. In DSS, the α phase is enriched with Cr and Mo, while the γ phase contains higher levels of Ni and N. However, it should be noted that EDS has limited sensitivity in detecting N, thus the mass fractions of N in the two phases are estimated. According to references[26,27] the content of N in the α phase is considered to be at saturation, approximately 0.05 wt.%. Given that the overall N content in 2205-A and 2205-B is 0.15 wt.%, the distribution of N in the γ phase can be calculated by considering the volume fraction of the total N content and γ phase in the alloy. Based on the above compositions, the PREN is calculated by formula (1)[5–8]:

$$\text{PREN} = \%\text{Cr} + 3.3\%\text{Mo} + 16\%\text{N} \tag{1}$$

In this equation, %Cr, %Mo, and %N are the mass fractions of Cr, Mo, and N, respectively, in the alloy.

PREN is frequently used as a direct measure of pitting resistance[28]. The phase ratio of 2205-B is more uniform, and the PREN values of its α and γ phases are comparably higher. Should the PREN be directly applied as the benchmark for evaluating pitting resistance, it would imply that 2205-B is expected to exhibit enhanced pitting resistance.

Electrochemical impedance spectroscopy

Figure 2 displays the electrochemical impedance spectroscopy (EIS) results. The Bode plots for both 2205-A and 2205-B exhibit two time constants, requiring the use of an equivalent circuit diagram with two time constants to fit the EIS data[29–31], as embedded in Fig. 2a. This equivalent circuit is considered to be the bilayer structure comprising of a porous outer layer and a relative compact inner layer[29]. R_S represents the solution resistance, R_1 is the diffusion resistance for ions across the outer layer and R_2 reflects the charge-transfer resistance. The constant-phase elements CPE_1 and CPE_2 correspond to the capacitive behavior of the outer layer and the electrochemical response of the electrical double layer at the end of the ion channels in the outer layer, respectively.

$CPE(Q, n)$ represents the constant phase element characterizing the frequency dispersion behavior arising from electrode surface heterogeneity. In accordance with this electrical equivalent circuit, the CPE_1 may exhibit a normal distribution of its time constant and the CPE_2 is typically regarded as having a surface distribution[32,33]. Hirschorn et al.[32] established a relationship between CPE parameters and effective

Fig. 1 | Duplex microstructures of 2205. **a**, **b** are optical morphologies of 2205-A after etching; (**c**) and (**d**) are 2205-B. **e** XRD diffraction pattern.
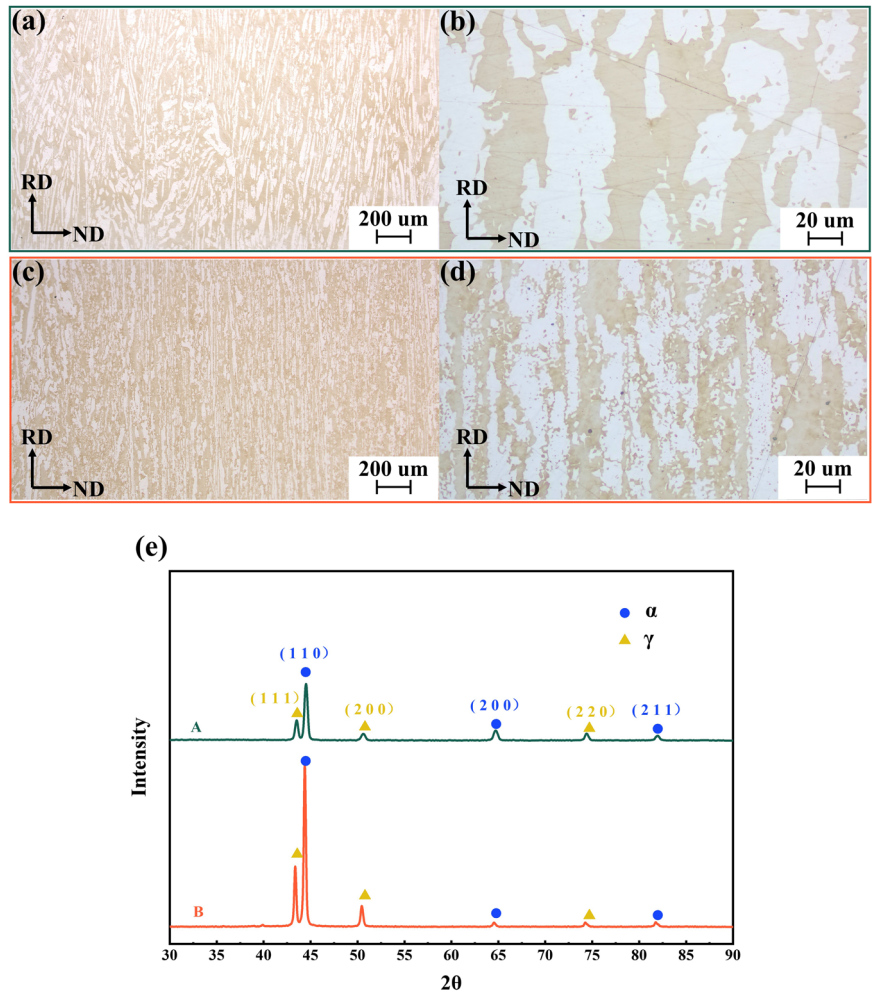
Table 2 | Two-phase ratio and alloying element content of 2205 DSS

Materials	Phase	Proportion %	Cr wt%	Mo wt%	Ni wt%	N wt%	PREN
2205-A	γ	41.82	19.87	2.04	6.26	0.28	31.23
	α	58.18	22.93	3.15	4.04	0.05	34.12
2205-B	γ	46.72	20.03	2.12	6.38	0.27	31.35
	α	53.28	23.16	3.38	4.02	0.05	35.11

capacitance ($C_{\mathrm{eff,PL}}$) based on the electrode admittance's characteristic time constant, expressed as follows:

$$C_{\mathrm{eff,PL}} = gQ(\rho_d \varepsilon \varepsilon_0)^{1-n} \tag{2}$$

$$g = 1 + 2.88(1 - n)^{2.375} \tag{3}$$

where Q and n are the CPE_1 parameters. ε represents the dielectric constant (15.6 for stainless steel passive film), ε_0 is the vacuum permittivity (8.85×10^{-12} F·m^{-1}), and ρ_d stands for resistivity with a designated value of 500 Ω m^{-1}. As for the surface distribution condition, Brug formula can be used to convert this CPE_2 into an effective capacitance ($C_{\mathrm{eff,surf}}$)[32]:

$$C_{\mathrm{eff,surf}} = Q^{1/n}(R_1^{-1} + R_2^{-1})^{(n-1)/n} \tag{4}$$

where Q and n are the CPE_2 parameters. The fitted R_2 values are larger than the R_1 values, indicating that the charge transfer is the dominant process in the electrochemical system of the passive film. Polarization resistance (R_p), commonly used to assess passive film protection performance[31], is calculated as follows:

$$R_p = R_1 + R_2 \tag{5}$$

Fig. 2 | The EIS results of different applied potentials in 85°C 1 M NaCl. a, c, e Nyquist and Bode of the 2205-A; (**b**), (**d**) and (**f**) Nyquist and Bode of the 2205-B; the equivalent circuit used in this work is embedded in (**a**).
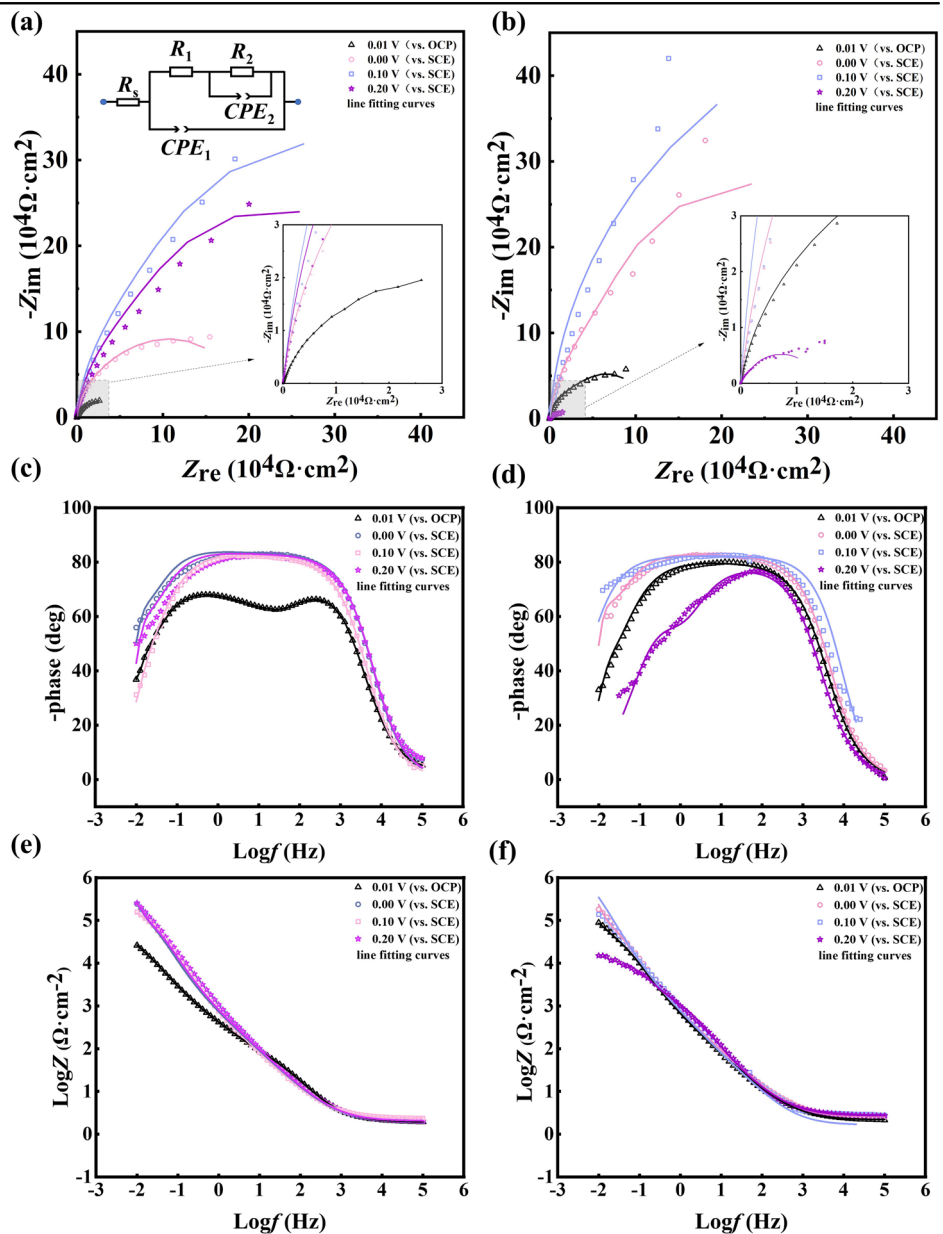
Table 3 | The EIS fitting results for 2205 in 1 M NaCl at 85 °C

Applied potential	R_S (Ω·cm²)	$Q_f Q_1$ (F·cm⁻²s⁻¹)	$Q_f Q_1$-n	CPE_1 (F·cm⁻²)	$R_f R_1$ (Ω·cm²)	$Q_t Q_2$ (F·cm⁻²·s^{n-1})	$Q_t Q_2$-n	CPE_2 (F·cm⁻²)	$R_t R_2$ (Ω·cm²)	R_p (Ω·cm²)
A-0.01 V (vs. OCP)	2.162	8.23×10^{-5}	0.96052	2.98775×10^{-5}	3.5261×10^4	1.40×10^{-5}	0.96522	1.34507×10^{-5}	6.8118×10^4	1.03379×10^5
A-0.00 V (vs. SCE)	2.142	6.56×10^{-5}	0.95838	2.25473×10^{-5}	8.8351×10^4	1.23×10^{-5}	0.98066	1.2201×10^{-5}	1.02250×10^5	1.90601×10^5
A-0.10 V (vs. SCE)	2.17	2.10×10^{-5}	0.98165	1.30910×10^{-5}	1.01360×10^5	9.30×10^{-6}	0.91840	8.96105×10^{-6}	2.33510×10^5	3.34870×10^5
A-0.20 V (vs. SCE)	2.06	5.47×10^{-5}	0.96850	2.43831×10^{-5}	9.7190×10^4	4.29×10^{-5}	0.91782	4.60518×10^{-5}	1.06420×10^5	2.03610×10^5
B-0.01 V (vs. OCP)	2.181	4.89×10^{-5}	0.97944	2.88519×10^{-5}	5.5155×10^4	1.05×10^{-5}	0.98145	1.02745×10^{-5}	7.1560×10^4	1.26715×10^5
B-0.00 V (vs. SCE)	2.546	2.57×10^{-5}	0.99315	2.15840×10^{-5}	8.8410×10^4	1.23×10^{-5}	0.91475	1.1733×10^{-5}	1.20260×10^5	2.08670×10^5
B-0.10 V (vs. SCE)	2.531	3.91×10^{-5}	0.96091	1.43457×10^{-5}	1.61180×10^5	2.28×10^{-6}	0.98598	2.22983×10^{-6}	2.60040×10^5	4.21220×10^5
B-0.20 V (vs. SCE)	2.693	6.30×10^{-5}	0.98891	4.74054×10^{-5}	1.2887×10^4	2.94×10^{-4}	0.89905	3.16292×10^{-4}	1.2903×10^4	2.5790×10^4

Table 3 displays the calculated R_p values of passive films at different potentials.

In the range from OCP to 0.10 V (vs. SCE), the arc radius of Nyquist and the R_p value of 2205-B are larger than 2205-A at the same applied potential, which indicates that the charge transfer resistance of 2205-B is greater and the passive film is more protective.

However, when the applied potential reached higher potential range (0.2 V vs. SCE), the R_p values of both specimens began to decline, especially for 2205-B. The transition indicates that 2205 DSS is in the potential range where pitting is possible, and the overall protection of the passive film decreases[30,31]. The potentiodynamic polarization curves (Fig. 3) also demonstrate that pitting will occur when the applied potential exceeds 0.2 V (vs. SCE) at 85 °C.

Based on the EIS results, it can be concluded that the passive film of 2205-B is more protective compared to 2205-A within a stable potential range, aligning with PREN result. However, as the EIS sinusoidal potential amplitude enters the pitting initiation range, 2205-B is more susceptible to pitting.

Critical pitting temperature

Through the polarization curve (Fig. 3), we found that 2205 DSS would transpassivate at low temperature (25 °C and 50 °C). At 85 °C, the potentials at which the currents of 2205-A and 2205-B rise are very similar. Since the potentiodynamic polarization curves are strongly dependent on the solution temperature, Critical Pitting Temperature (CPT) is a better method to compare these two specimens. The CPT test serves as an efficient means to evaluate the pitting resistance of stainless steel. To counterbalance the inherent randomness of pitting events, we performed 15 valid CPT measurements on both 2205-A and 2205-B, as shown in Fig. 4a. The lowest CPT values for both 2205-A and 2205-B were identified to be 47 °C. However, the CPT measurements for 2205-A showed a range of 18 °C, whereas for 2205-B, the range was narrower at 12 °C. The average CPT value and standard deviation of 2205-A (57.7 ± 4.6 °C) are greater than 2205-B (54.2 ± 2.6 °C). When the temperature approached the CPT, there were almost no metastable pitting occurrences observed in the current of 2205-A, whereas 2205-B exhibited a small number of metastable fluctuations. Figure 4b displays the cumulative probability distribution of CPT values, which was calculated by Eq. (6)[34]:

$$P(E) = \frac{n}{(N+1)} \qquad (6)$$

In the given formula, N represents the total number of measurements (15 in this case), and n represents the number of individual CPT measurements included in each measurement. To effectively compare the pitting resistance of 2205-A and 2205-B, the median of the cumulative probability is considered, which corresponds to the temperature where $P(E) = 0.5$. As illustrated in Fig. 4b, the median CPT value of 2205-A is 57.9 °C, which is higher than that of 2205-B, which is 54.2 °C.

Figure 4 indicates a wide distribution of CPT values, which is consistent with the findings reported by Peguet[35]. Following Frankel's "passive film breakdown vs. pit growth stability" pitting framework[19], when the key controlling step in pitting is the initiation, the lower the initiation probability, the greater the measured discreteness in CPT values ($\triangle CPT_{freq}$).

In the case of 2205-A and 2205-B, it can be inferred that the pitting initiation for both types is difficult, and the initiation probability for 2205-A is even lower than that of 2205-B. This lower initiation probability contributes to higher values and a wider distribution of CPT.

It's worth emphasizing that, based on EIS data, the passive film of 2205-B exhibits superior stability. This implies fewer initiation events in 2205-B. Such a discrepancy necessitates a more detailed exploration of the initiation processes for both 2205 specimens, as will be discussed in subsequent sections.

Fig. 3 | Typical potentiodynamic polarization curves of 2205 DSS at different temperatures in 1 M NaCl.
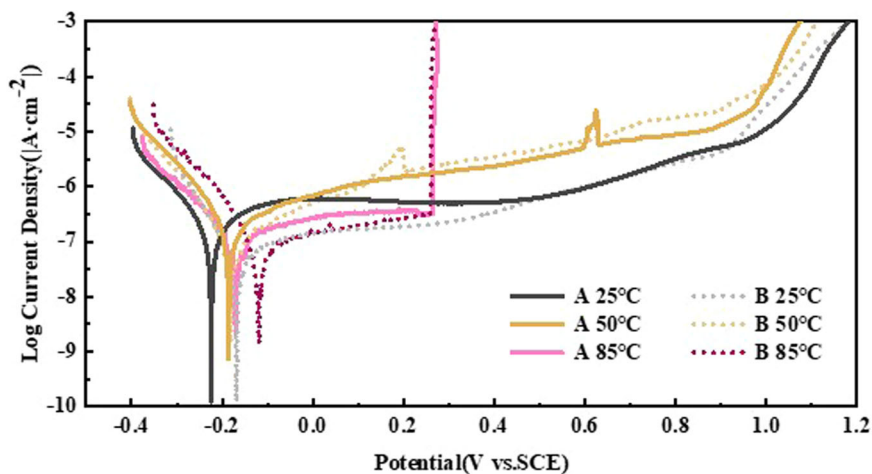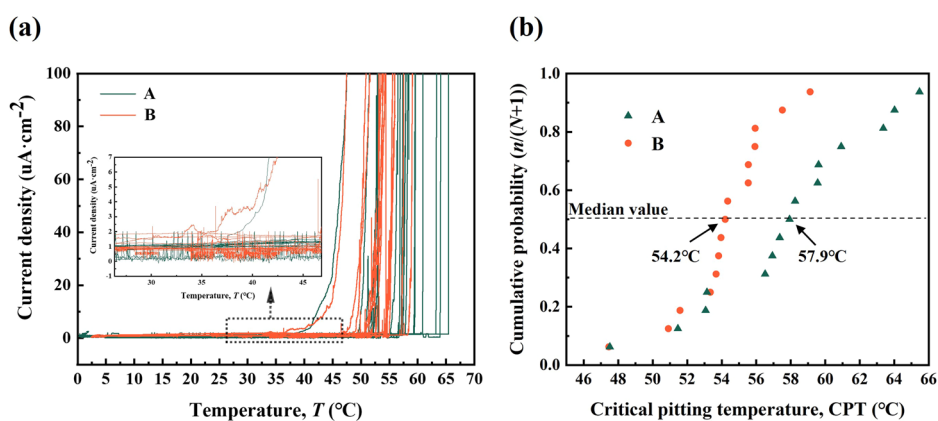

Fig. 4 | Potentiostatic CPT (applied potential 700 mV vs. SCE) in 1 M NaCl solution. a current-temperature curve and partial magnification; (**b**) cumulative probability distribution of CPT values and the median values are ~58 °C (2205-A) and ~54 °C (2205-B).

Potentiostatic pulse test

The PPT has demonstrated its efficacy in stimulating pitting in stainless steel. During the high potential stages of the initial cycles (Fig. 5a), both 2205-A and 2205-B exhibit significant peaks of current density, which indicates the occurrence of stable pits in active sites[36]. Furthermore, based on the current curves, more frequent fluctuations or spikes are observed in 2205-B, suggesting a higher incidence of pitting initiation. Optical microscope (OM) observations reveal a disparity in pit count between the two specimens: approximately 21 for 2205-A and around 93 for 2205-B, as shown in Fig. 5b, c. (Due to the limited resolution of the OM stitching, a very small number of small size pits less than 20 μm in diameter and less than 4 μm in depth are ignored). Then the size of the pits after PPT were measured by a confocal laser scanning microscope (CLSM), as shown in Fig. 5d. The two types of 2205 pits nearly equivalent in average size. The average pit depth of 2205-A (~18 μm) in Fig. 5e is slightly lower than that of 2205-B (~21 μm) in Fig. 5f. There is no significant difference between the average pit length and width of 2205-A (~144 × 133 μm) and 2205-B (~149 × 134 μm).

Potentiostatic polarization

To gain a deeper understanding of metastable pitting behavior, we conducted potentiostatic polarization tests (PSP) on both 2205 specimens. Each specimen was tested ten times, and representative current curves from these tests are presented in Fig. 6.

In general, the passive film of each specimen is stable as the current density maintains at a low level. However, occasional occurrences of metastable fluctuation currents are observed. Specifically, 2205-A exhibits approximately 22 metastable current fluctuations across 10 potentiostatic polarizations, while 2205-B has around 82 fluctuations. Through a statistical

analysis of these peaks, we derived the cumulative probability distributions for both I_{peak} and Q, as illustrated in Fig. 7.

The cumulative probability of metastable pitting peak current I_{peak} is shown in Fig. 7a. I_{peak} is the difference between the highest current and the baseline current during metastable pitting. We still choose the corresponding value of P(E) = 0.5 for comparison. The median peak current of 2205-A (~0.56 μA) is lower than that of 2205-B (~1.99 μA).

Simultaneously, by integrating the metastable fluctuation current over the duration of pit growth, we obtain the electric charge, Q, associated with the metastable pit. Working under the assumption that these metastable pits develop in a hemispherical fashion, as delineated in ref. 37, we can determine the radius of each metastable pit employing Faraday's law, as endorsed by studies[38,39]. The formula (7) facilitates the computation of the radius (a) for these pits:

$$a = \left(\frac{3ZQ}{2\pi nF\rho}\right)^{\frac{1}{3}}$$ (7)

In this study, the primary dissolved elements were Fe, Cr, and Ni. The respective values for Z (the molar mass), n (the oxidation state of the dissolved cation), and ρ (the density of 2205) were 55.00 g·mol^{-1}, 2.26, and 7.754 g·cm^{-3}, respectively[40]. F represents Faraday's constant, which is 96485 C·mol^{-1}. The median pit radius for 2205-A was found to be approximately 1.66 μm, while for 2205-B, it was around 4.18 μm as shown in Fig. 7b.

To better reveal the growth stability of metastable pitting, the pitting stability product i·a is considered, as documented in various studies[41–46]. This product, defined as the multiplication of the pit depth a and the pit current density i, acts as a metric for growth stability. A higher value of i·a for an
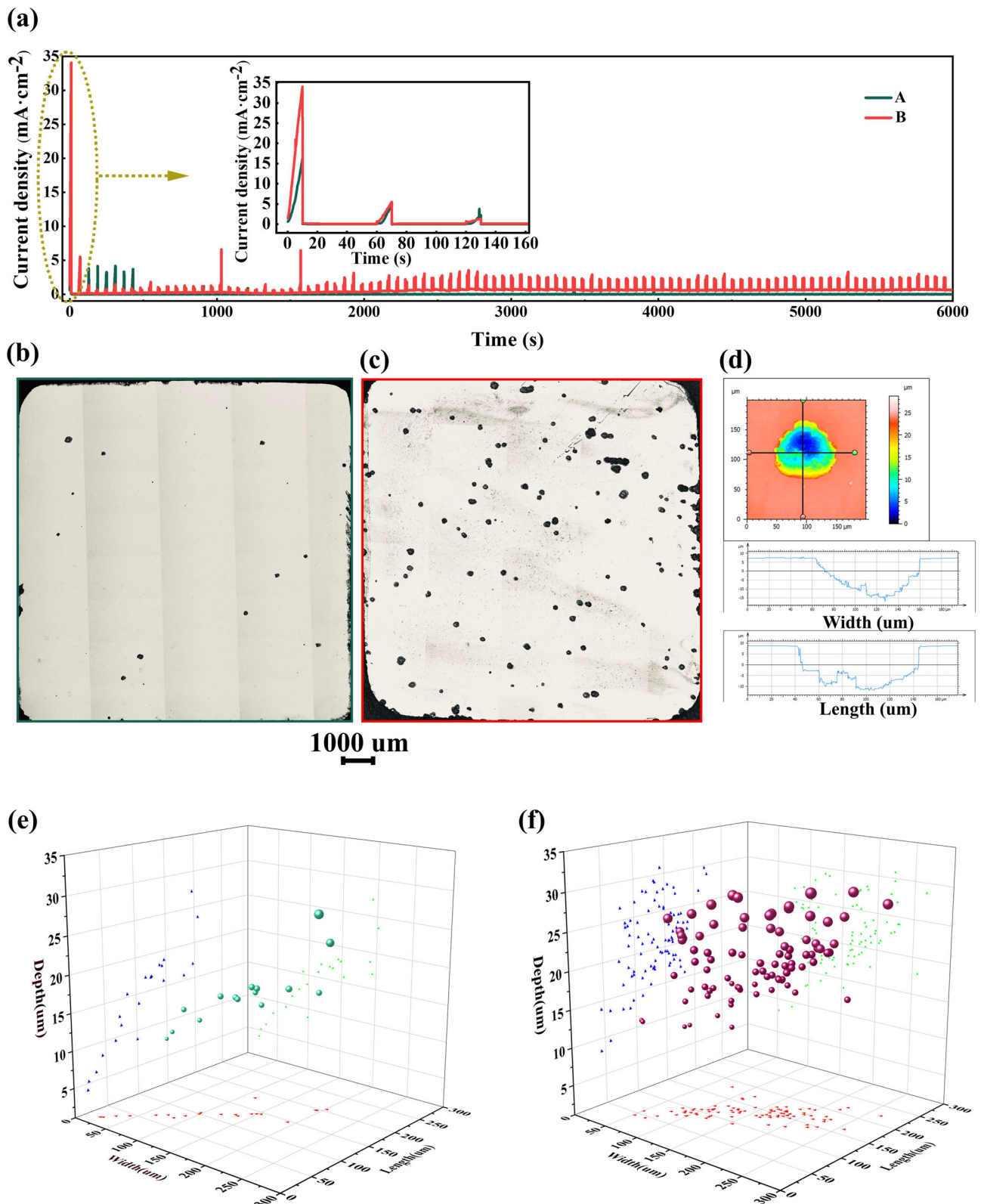
Fig. 5 | Potentiostatic pulse tests (85°C 1 M NaCl solution, high potential 0.85 V was applied for 10 s and low potential 0 V for 50 s). a current curves of potentiostatic pulse tests; macro morphologies of 2205-A (**b**) and 2205-B (**c**) after PPT; (**d**) schematic diagram of measuring the length, width, and depth of the pit using a laser confocal microscope; pits size statistics of 2205-A (**e**) and 2205-B (**f**) after PPT.

individual pit suggests a higher likelihood of it meeting the critical conditions necessary for sustained growth[47].

For our analysis, the current density i is calculated by dividing the peak current (I_{peak}) by the metastable pit's hemispherical surface area ($2\pi a^2$).

Then the stability product i·a can be obtained by:

$$i \cdot a = \frac{I_{peak}}{2\pi a} \tag{8}$$

Fig. 6 | Typical current curves from the potentio-static polarization tests in 1 M NaCl solution at 50 °C and 0.2 V (vs. SCE) as constant potential for 2205-A and 2205-B specimens.
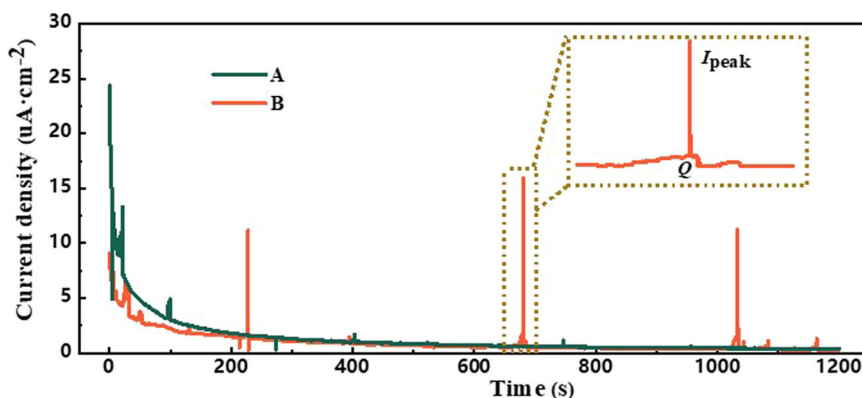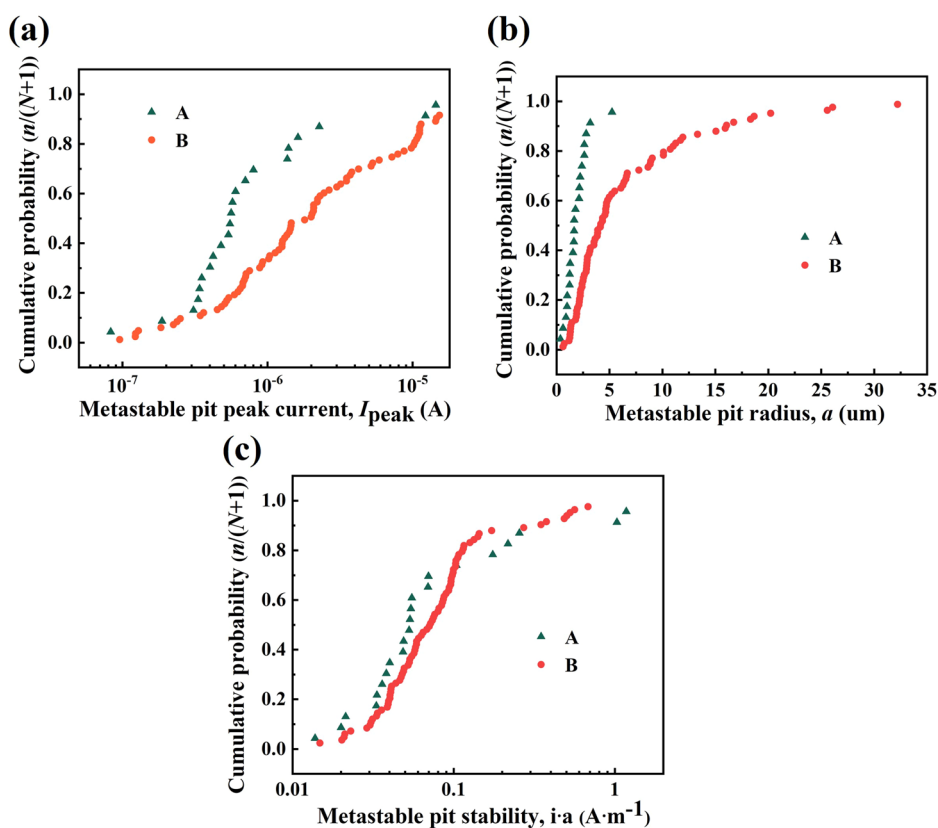

Fig. 7 | Potentiostatic polarization tests (1 M NaCl solution at 50°C and 0.2 V vs. SCE as constant potential) statistics. a metastable current peak; (**b**) metastable pit radius; (**c**) cumulative probability distribution of metastable pitting stability product.

The median value of the stability product i·a for 2205-A (~0.053 A·m^{-1}) approximates that of 2205-B (~0.072 A·m^{-1}), as illustrated in Fig. 7c. The pitting growth stability of the two types of 2205 is very similar. The PSP experiments further confirm that the reason for the lower pitting resistance of 2205-B compared to 2205-A is its higher initiation frequency, which aligns with the previously mentioned PPT results.

Analysis on initiation

Pitting initiation typically stems from surface defects such as dislocations, phase boundaries[48,49], heterogeneous particles[50,51] and local heterogeneities of passive film[17,18]. The impurities found in DSS during smelting primarily come from the sulfide and oxide residues of the argon-oxygen decarbonization refining process, along with composite products formed during desulfurization and deoxidation. These inclusions can be categorized based on their composition into groups such as oxide inclusions, sulfide inclusions, silicate inclusions, calcium aluminate inclusions, and so on.

The pitting mechanism, influenced by diverse inclusions, varies accordingly. For complex inclusions containing sulfur elements, such as MnS and CaS, they form galvanic corrosion couples with the surrounding matrix due to their relatively lower electrochemical potential in comparison to the matrix, leading to their preferential dissolution. The behavior of oxide inclusions, however, is more complex. A potential electrochemical interaction might occur between the oxide and its surrounding substrate. Zheng et al.[52] identified that the surface potential of inclusions formed by (Mg-Al-Ca)-O was lower than that of the surrounding substrate. They postulated that in a solution abundant with sulfur and chlorine, such inclusions could initiate galvanic corrosion at their periphery. On the other hand, some researchers have posited that oxide inclusions act as insulators, which would prevent the formation of a galvanic couple between these oxide inclusions and the surrounding matrix[53,54]. Owing to their thermodynamic instability, oxide inclusions can undergo a chemical dissolution process during the early stages of pitting initiation. For example, Kim et al.[55] reported that a (Ca-Si)-O inclusion might dissolve in an environment with NaCl, leading to
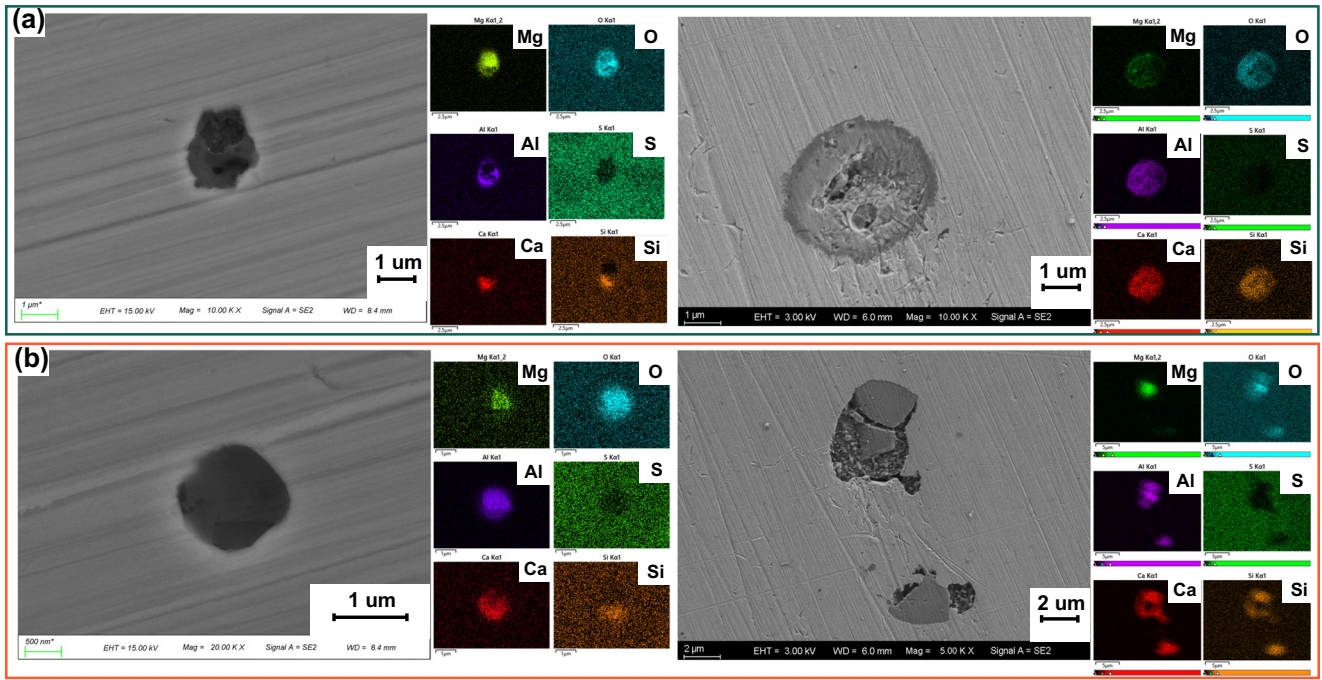
Fig. 8 | Typical structure and composition of complex oxide inclusion observed by SEM-EDS. a 2205-A at 15 kV (left) and 3 kV (right); (**b**) 2205-B at 15 kV (left) and 3 kV (right).
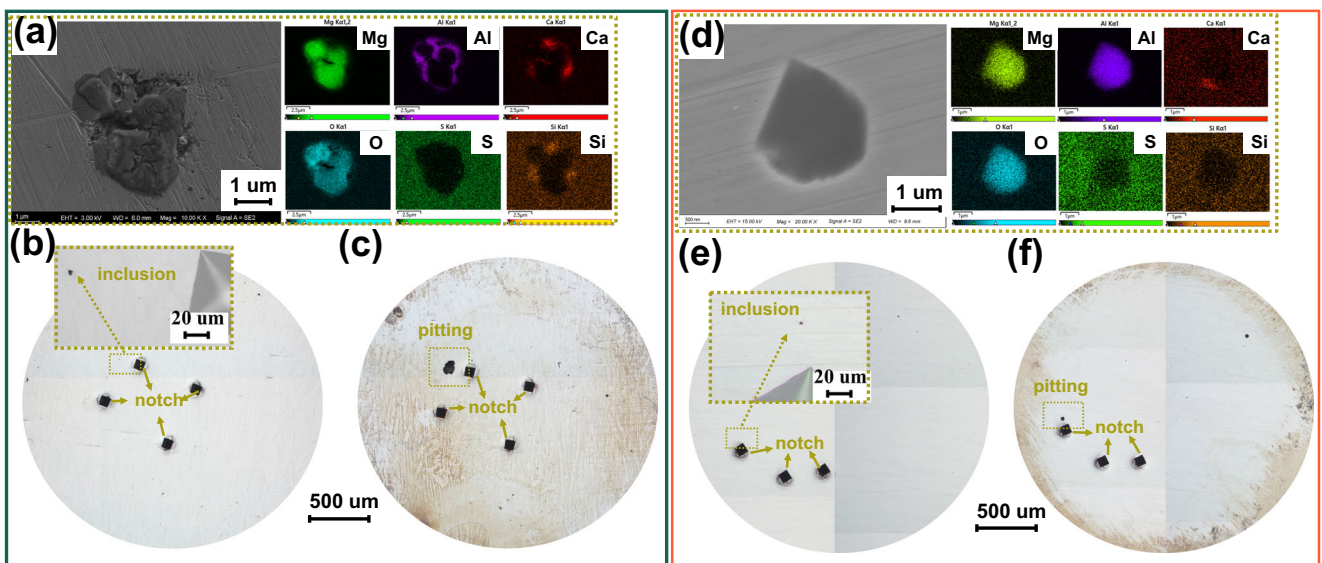

Fig. 9 | Comparison of 2205 exposed surface before and after PPT (85 °C 1 M NaCl electrolyte, high potential 0.85 V was applied for 10 s and low potential 0 V for 50 s). **a−c** is 2205-A; (**d−f**) is 2205-B; Where: (**b**, **e**) before the PPT; (**c**, **f**) after PPT; (**a**, **d**) EDS mapping of inclusion components for pitting.

pitting in 316 L stainless steel. Muto et al.[56] asserted that the CaO and MgO within complex oxide inclusions could dissolve in water, causing the entire inclusion to detach from the matrix. Additionally, certain researchers proposed that pitting can stem from the dissolution of substrate regions that are highly distorted, especially in areas adjacent to oxide inclusions[57]. In summary, the complex oxide inclusions undermine the uniformity of the passive film, and the inclusions dissolution amplifies the susceptibility of substrate to pitting initiation[58].

Oxide inclusion characteristics of 2205

Scanning electron microscopy equipped with energy-dispersed spectroscopy (SEM-EDS) analysis revealed that the predominant heterogeneous particles in both 2205-A and 2205-B were oxide inclusions, as illustrated in Fig. 8. These inclusions primarily comprise elements of (Mg-Al-Ca-Si)-O, potentially sourced from smelting residues of deoxidizing agents like Mg, Al, Ca and Si[59–64]. Within the inclusion, MgO often manifests as an irregular polygonal structure (as depicted in Fig. 8a left). When combined with Al_2O_3, it forms the Mg-Al spinel, which undergoes a transition to a more rounded shape. Along the edge of the inclusion, a certain amount of $CaSiO_3$ can also be detected. When the concentration of $CaSiO_3$ escalates, it tends to envelop the entire inclusion particle (Fig. 8a right). Consequently, a complex inclusion can be roughly divided into MgO, (Mg-Al)-O, and (Ca-Si)-O parts. However, the boundaries delineating these parts are not always discernible.

Given the diminutive size of the inclusion, often less than 5 μm, the information obtained from EDS may be insufficient to reveal the intricate
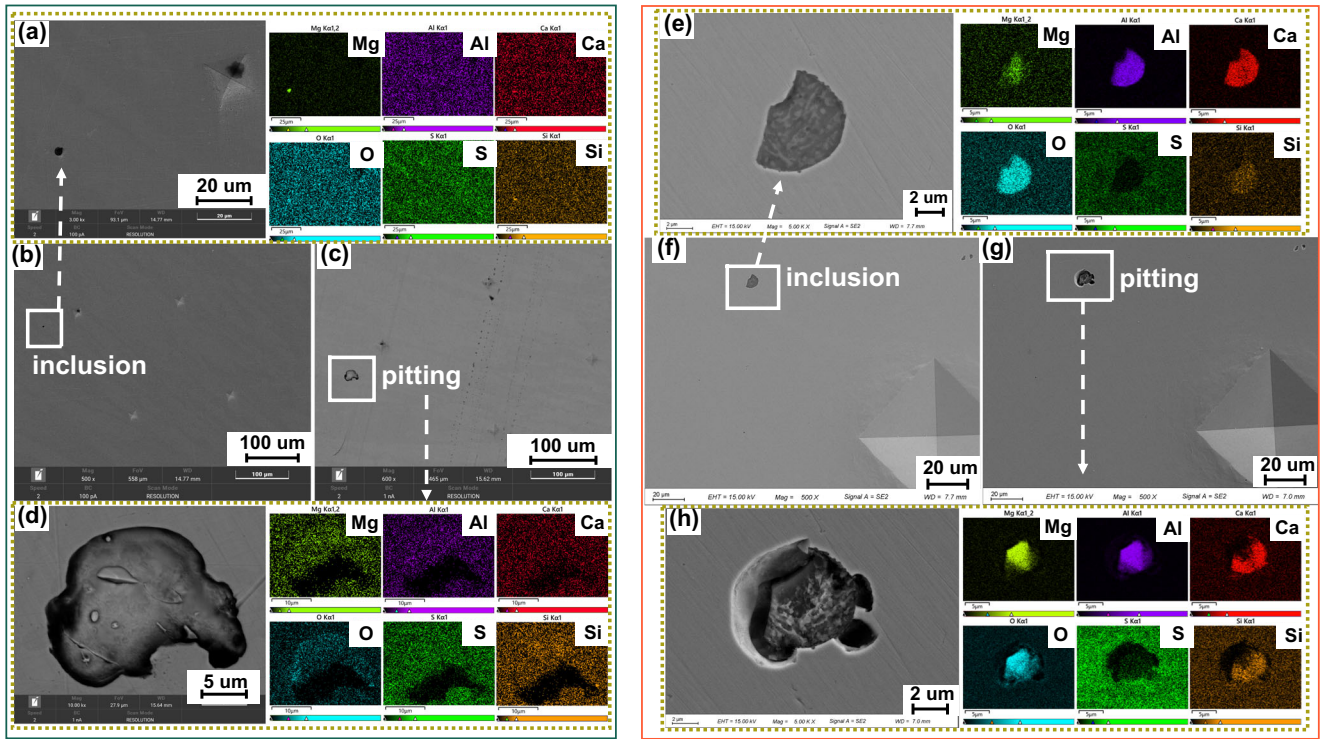
Fig. 10 | Comparison of inclusion before and after PPT (85 °C 1 M NaCl electrolyte, high potential 0.85 V was applied for 0.1 s and low potential 0 V for 2 s). a−d is 2205-A; (e−h) is 2205-B; Where: (b, f) before PPT; (c, g) after PPT; (a, e) EDS mapping of inclusions; (d, h) EDS mapping of pits initiated by corresponding inclusions.
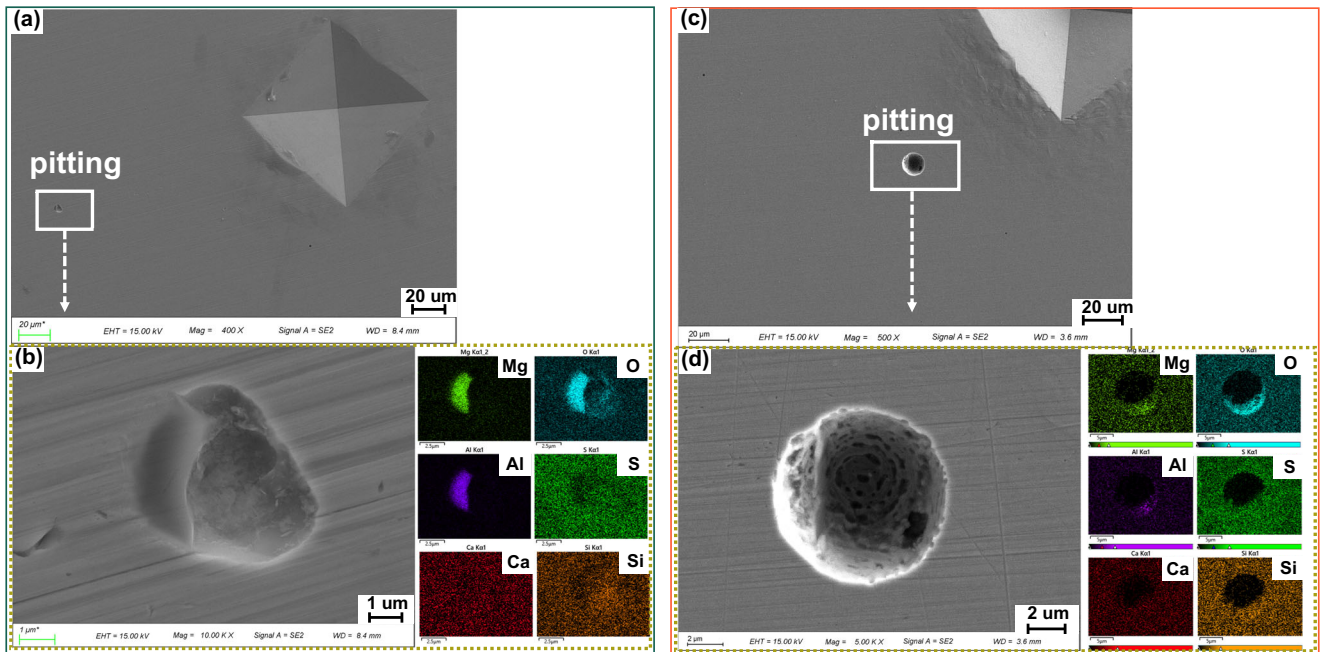

Fig. 11 | Residual composition in pits. a, b 2205-A; (c, d) 2205-B, where: (a, c) is the location of the notch corresponding to the pit; (b, d) represents the pit morphology and residual composition.

internal structure. Consequently, the inclusion may appear homogeneously rich in (Mg-Al-Ca-Si)-O components throughout.

Influence of oxide inclusion on pitting initiation

To delve deeper into the possible influence of oxide inclusions on pitting initiation in both 2205-A and 2205-B, we carried out PPT experiments on the specimen with a diameter of 3 mm (as depicted in Fig. 9). In such a small area it is easier to locate some specific inclusions and compare their compositions and structures before and after corrosion. Initially, the exact position of the inclusion was pinpointed through OM (Fig. 9b). To further authenticate its composition, detailed analysis was done using SEM-EDS (Fig. 9a). Subsequently, the specimen was subjected to PPT and then was observed again by OM and SEM-EDS.
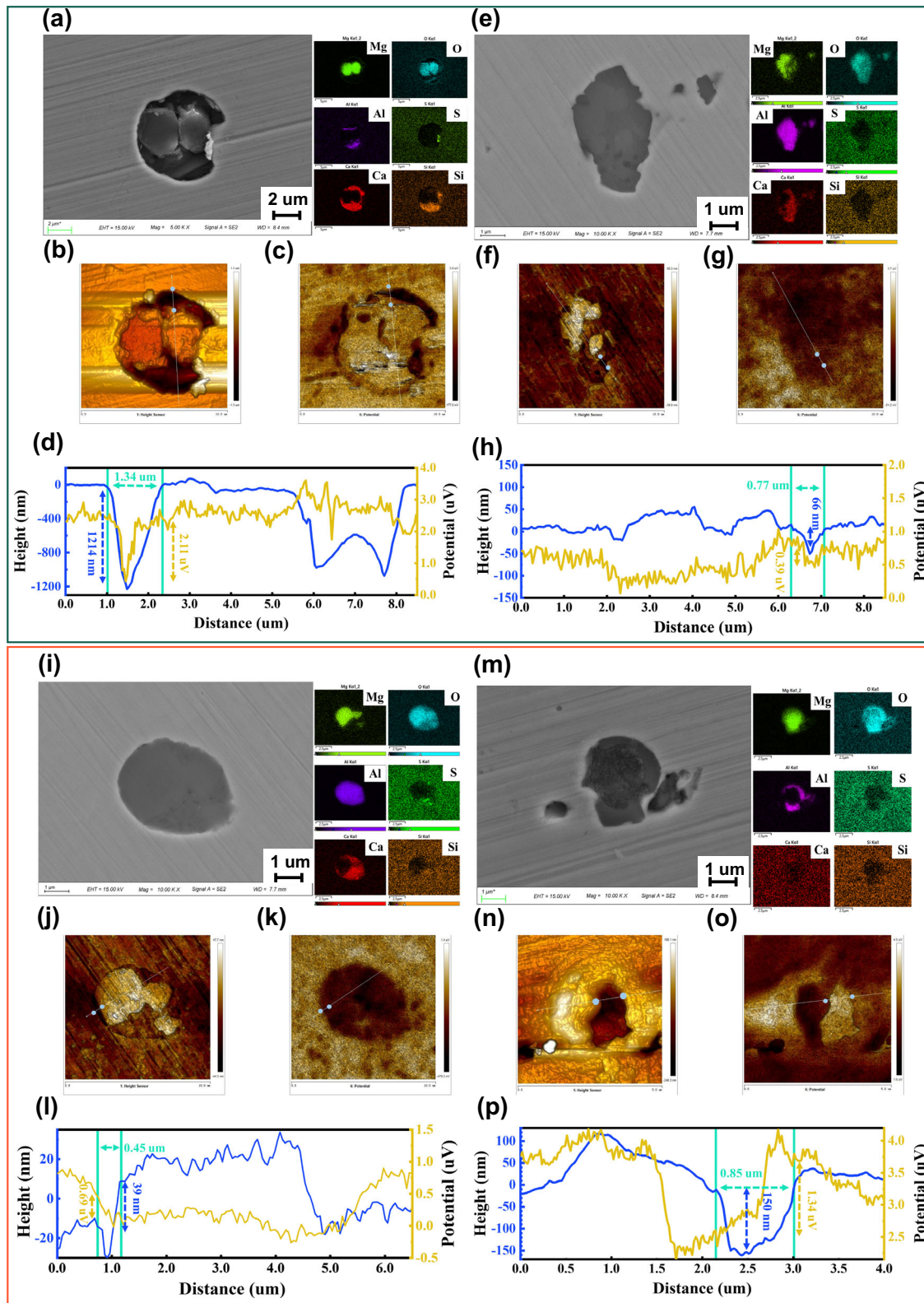
Fig. 12 | Morphology of oxide inclusion and corresponding surface height and volt potential in 2205. a–h is 2205-A; (**i–p**) is 2205-B; Where: (**a, e, i, m**) are the SEM morphology of the inclusion and the corresponding EDS mapping; (**b, f, j, n**) refers to the surface height of the inclusion; (**c, g, k, o**) refers to the inclusion surface voltages; (**d, h, l, p**) are the height and voltage changes corresponding to the line sweep portion of SKPFM.

After PPT, 2205-A exhibits a sole stable pit at the marked inclusion adjacent to the notches (Fig. 9c). Similarly, the oxide inclusion in 2205-B (Fig. 9d, e) also initiates pitting (Fig. 9f).

It is noteworthy that capturing all inclusions under SEM is challenging, particularly in areas distant from the notches. Another

pit can be observed in the upper right part of 2205-B. The presence or absence of oxide inclusion at this site was not recorded before PPT. Nonetheless, it's reasonable to infer that in both types of 2205, the primary culprits for pitting initiation are the complex oxide inclusions.

Fig. 13 | Initiation mechanism of pitting of 2205 DSS triggered by oxide inclusion. a the Ca-Si-O part of the complex inclusions is depressed due to the original dissolution of CaO; (**b**) the stainless steel encounters a Cl⁻ environment; (**c**) rapid dissolution of Ca-Si-O leads to corrosion of the surrounding matrix, and Mg-Al-O gradually dissolves in an acidic environment; (**d**) Ca-Si-O completely dissolved and steady-state pitting formed.
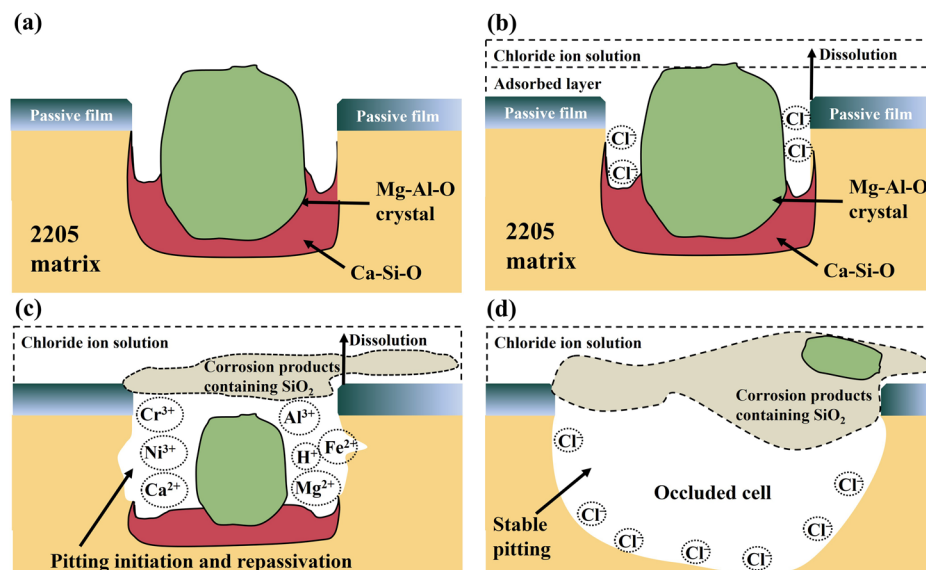
Inclusion residue after PPT

To achieve a detailed analysis of the pitting process, we adjust the parameters of PPT to preserve the residual composition of inclusions within the pits. The durations of E_h and E_l were set 0.1 s and 2 s, respectively.

Before PPT, the inclusion (Fig. 10b) in 2205-A predominantly showed a composition rich in (Mg-Al-Ca-Si)-O elements (Fig. 10a). After PPT, this inclusion led to the formation of an irregular pit (Fig. 10c) containing residual Mg-Si-O elements.

In a parallel observation, 2205-B exhibited a comparable trend. Before PPT, a notable semi-circular inclusion, predominantly composed of (Mg-Al-Ca-Si)-O elements, was identified (Fig. 10g). After PPT, the resulting pit highlighted the selective dissolution of the (Ca-Si)-O constituents, thereby exposing an internal triangular (Mg-Al)-O spinel structure (Fig. 10h).

This phenomenon is universal when we observe more pits on the specimens. Residual analysis of pits in both 2205-A (Fig. 11a, b) and 2205-B (Fig. 11c, d) showed remnants of (Mg-Al)-O and SiO₂, which suggest that calcium-enriched constituents are more vulnerable to dissolution during the pitting process.

Scanning kelvin probe force microscopy results of inclusions

To elucidate the specific mechanism through which these complex oxide inclusions initiate pitting, we utilized scanning kelvin probe force microscopy (SKPFM). This allowed us to accurately gauge the height and surface voltages of two distinct inclusions in both 2205-A (Fig. 12a−h) and 2205-B (Fig. 12i−p). (Mg-Al)-O exhibits enhanced hardness and thermodynamic stability relative to (Ca-Si)-O. As a consequence, (Ca-Si)-O might undergo slight dissolution during the polishing process[65]. This results in a discernible height variation between (Ca-Si)-O and (Mg-Al)-O, as shown in Fig. 12b, f, j, n. Typically, these recessed areas coincide with a decrease in surface potential. For instance, within the oxide inclusion of 2205-A (Fig. 12a), the width of (Ca-Si)-O is around 1.34 μm. The height difference between (Ca-Si)-O and (Mg-Al)-O is roughly 1214 nm, associated with a decrease of 2.11 μV in surface potential (Fig. 12d). The inclusions observed in 2205-B follow a similar trend. It should be noted that these surface potential values are also influenced by the size of the inclusion and the primary oxide layer on the surface[66–68].

Discussion

While previous studies largely suggest that the probability of forming a galvanic corrosion couple between the oxide inclusion and the steel matrix remains minimal[69,70], there's still a possibility for such couples to form internally within the inclusions. This could instigate pitting through a synergistic effect of electrochemical and chemical reactions[53,54,71,72]. Based on the experimental results and the subsequent analysis, the mechanism of pitting initiation triggered by complex oxide inclusion appears consistent across both types of 2205, as depicted in Fig. 13.

Initially, the thermodynamically unstable Ca-containing part exhibit a propensity for preferential dissolution, while SiO₂, MgO, and Al₂O₃ are stable[54]. Mechanical processes like water grinding or polishing may induce the partial dissolution of CaO[65], resulting in the surface depressions of Ca-Si-O segment and leaving the Mg-Al-O segment convex (Fig. 13a). When the stainless steel encounters a Cl⁻ environment, the potential of the (Ca-Si)-O drops, making it more anodic compared to its neighboring (Mg-Al)-O. This initial anodic dissolution leads to subsequent corrosion, as illustrated in Fig. 13b.

As the corrosion propagates, hydrolysis of Ca^{2+} produces H^+, which accentuates local corrosion and thereby accelerates the dissolution of Ca. Part of the new surface will continue to dissolve in the acidic environment, while other parts will be passivated. With the increasing dissolution of (Ca-Si)-O, the ion diffusion from the bottom of the crevice into the bulk solution becomes increasingly difficult. The potential difference between the bottom and the opening continues to rise until the potential at the crevice bottom falls below the stable potential of the passive film (IR drop effect)[73]. In these small crevices, a substantial amount of Ca^{2+} accumulates, accompanied by Fe^{2+}, Ni^{2+}, Cr^{3+} originating from matrix dissolution. Moreover, as crevices become saturated with HCl, the (Mg-Al)-O segment may also dissolve gradually. The hydrolysis of these cations further depresses the pH, and the continuous ingress of chloride ions into the pit to uphold electrical neutrality intensifies this hydrolysis[74] as visualized in Fig. 13c.

Ultimately, when the portion containing Ca has dissolved entirely, the remnant (Mg-Al)-O detaches and blends with SiO₂ among the corrosion products (Fig. 13d). By this stage, the pit holds a high chloride ion concentration. The simultaneous occurrence of active dissolution and passivation results in an irregular pit morphology. This steady-state pitting can maintain its growth through autocatalytic reactions in a confined environment[75,76]. According to our results and the refs. [22,77], the stability is related to the composition of Ca in the inclusion. The higher the Ca content, the more susceptible it is for the inclusion to dissolve, leading to stronger aggressiveness inside the pit and easier steady-state propagation.

While the initiation mechanisms in both types of 2205 appear similar, variations in their pitting resistance can be attributed to other factors. To delve deeper into this disparity, we conducted further statistical analysis of the inclusions identified in both types of 2205.

Fig. 14 | Statistical difference of inclusions in two 2205. a Comparison of inclusions quantity and size. Ternary phase diagram of the composition of 2205-A (**b**) and 2205-B (**c**) complex oxide inclusion (Mg-Al-Ca).
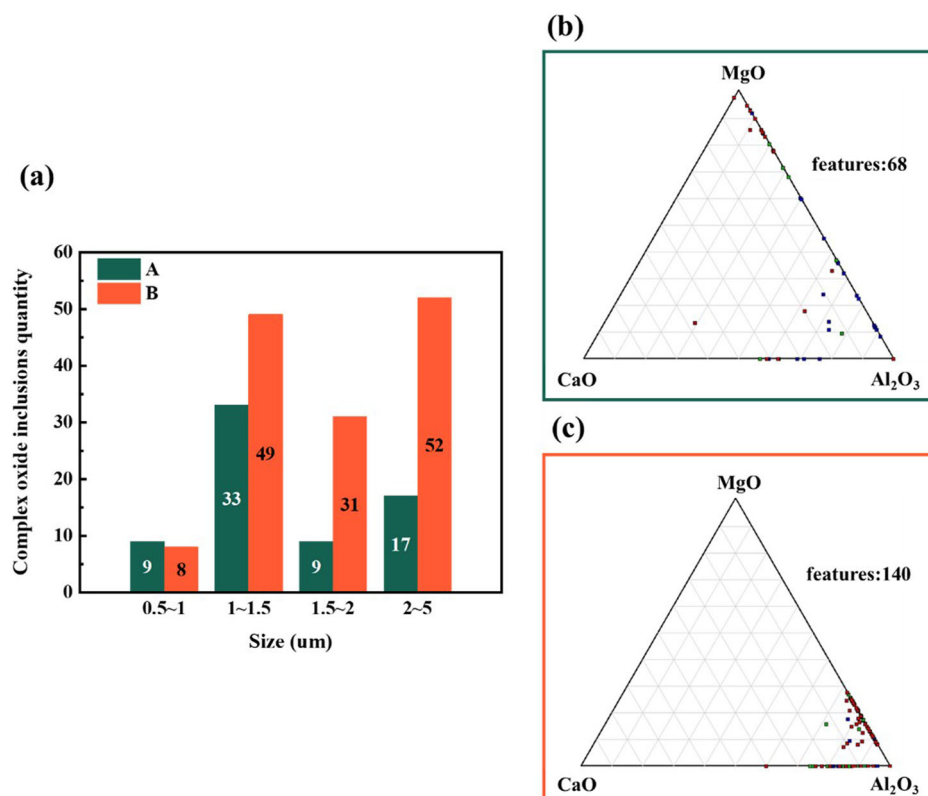
MnS and its complexes have been traditionally identified as pitting initiation sites[78–82]. However, with advancements in sulfur control technology, the sulfur content in the investigated 2205 DSS has been kept exceptionally low (<0.001 wt%). From our prior experiments, we did not identify any sulfide inclusions in the specimens.

SEM was employed to evaluate the inclusions of both two types of 2205, as illustrated in Fig. 14a. Heterogeneous particles observed in the SEM of both 2205-A and 2205-B were identified as complex oxide inclusions, which is consistent with the findings presented in Figs. 8–12. There are 68 oxide inclusions in the 2205-A scanning area and 140 in the 2205-B scanning area. All inclusions sizes fall within the range of 0−5 μm. In the smaller particle range of 0.5−1 μm, the number of inclusions in both 2205-A and 2205-B is comparable. However, in the ranges of 1−1.5, 1.5−2, and 2−5 μm, 2205-B contains more inclusions.

The proportions of the (Mg-Al-Ca) components in the oxide inclusions were statistically represented on a ternary phase diagram (Fig. 14b, c). When the CaO content is too small or non-existent, the particles in the ternary component are positioned along the MgO-Al$_2$O$_3$ axis. It is believed that MgO and Al$_2$O$_3$ are thermodynamically stable and difficult to dissolve chemically[56,58,72]. Meanwhile, MgO and Al$_2$O$_3$ are insulators and cannot form the galvanic couple with the substrate[53,54]. Therefore, they do not play a role in pitting initiation. It is evident that 2205-A contains only approximately 18 CaO-containing components, whereas 2205-B exhibits around 66 CaO-containing components. This discrepancy correlates well with the disparity in the count of steady-state pits illustrated in Fig. 14b and the difference in the number of metastable pits shown in Fig. 7. Specifically, the number of initiation sources (Ca-containing oxide inclusions) in 2205-B is approximately three to four times greater than that in 2205-A.

The aforementioned analysis elucidates the variance in CPT observed between the two types of 2205, which deviates from predictions grounded on PREN. Although 2205-B possesses a superior PREN value, the greater number of Ca-containing oxide inclusions in 2205-B heightens the probability of pitting initiation. As a result, the CPT of 2205-B is lower, and a larger number of steady-state and metastable pits manifest through PPT and PSP experiments.

This study aimed to evaluate the pitting resistance of two types of 2205 duplex stainless steels using various methods. The findings indicate that the initiation process is the key factor in pitting. Simply comparing Pitting Resistance Equivalent Number values does not fully explain the differences in pitting resistance. The specific conclusions drawn from this study are as follows:

1. Despite having a higher Pitting Resistance Equivalent Number value, 2205-B exhibits a lower Critical Pitting Temperature value. Moreover, the results of the potentiostatic pulse test and potentiostatic polarization demonstrate a larger number of pitting initiation sites on the surface of 2205-B.
2. Pitting initiation in both types of 2205 can be attributed to the preferential dissolution of Ca-containing parts in the (Mg-Al-Ca-Si)-O complex inclusions. 2205-B contains a higher quantity of Ca-containing oxide inclusions, which increases the likelihood of pitting initiation and subsequently reduces its pitting resistance.
3. The potentiostatic pulse test proves to be a tool for identifying the sources of pitting initiation and investigating the mechanism behind it. It retains early-stage information about pitting initiation and enables statistical evaluation, thereby facilitating a deeper understanding of the process.

These conclusions emphasize the importance of considering factors beyond Pitting Resistance Equivalent Number values when evaluating the pitting resistance of duplex stainless steels.

Methods
Specimen preparation
The specimens used were in the form of fabricated sheets and did not undergo any additional heat treatment. Test specimens were prepared by cutting square sections of dimensions 12 × 12 × 4 mm. The original exterior surface was retained as the testing surface, set aside for subsequent polishing.

The surface oxide was removed using silicon carbide sandpaper, and a copper wire was attached through tin welding to the opposite side of the original surface. The test specimen was then placed face down into a PVC plastic tube and embedded in epoxy resin. Subsequently, a series of wet grinding processes were conducted using 80#, 180#, 600#, 1000#, and 2000# silicon carbide grinding sandpaper, followed by polishing with 2.5 μm diamond polishing paste. After the ultrasonic cleaning with alcohol and drying, the specimen was affixed with electric insulation tape to leave a certain surface area exposed. It is important to note that, unless specifically mentioned, the exposed area of the specimens for measurement was maintained at 1 cm^2.

Electrochemical experiments

All electrochemical experiments used the standard three-electrode system of saturated calomel electrode (SCE) as the reference electrode, platinum electrode as the auxiliary electrode, and the specimen to be tested as the working electrode. The electrolytic cell employed was a glass beaker, and a 1 mol·L^{-1} NaCl solution served as the electrolyte for all electrochemical experiments. The ratio of electrolyte volume to the test area of the specimen exceeded 200 mL·cm^{-2}. Prior to all electrochemical experiments, the specimen was cathodic polarized at a potential of -900 mV (vs. SCE) for 2 min and conducted an open-circuit potential (OCP) test for 1800 s.

The Critical Pitting Temperature (CPT) test was conducted as follows: The specimen was immersed in a NaCl solution at 0 °C. After cathodic polarization and OCP, the specimen was subjected to potentiostatic anodic polarization at 700 mV (vs. SCE). Upon a gradual current density increase of 10^{-7} A·cm^{-2}, the solution was heated at a constant rate of 1 °C·min^{-1}. The electrochemical workstation, interfaced with a computer, recorded the current density-temperature curve in real-time during testing. When the current density sharply escalated to 100 μA·cm^{-2} and continued increasing, the corresponding temperature was designated as the CPT. The experiment halted when the current density rose to 1.5 mA·cm^{-2}. Upon completion of the experiment, the test surface of the specimen was inspected under an optical microscope to analyze the pitting morphology. If crevice corrosion was detected at the edge or any other location, the CPT results were considered invalid.

The potentiodynamic polarization curve was scanned positively from -0.25 V (vs. OCP) to 1.2 V (vs. SCE) at a rate of 10 mV·min^{-1} in 1 M NaCl solution at different temperature after cathodic polarization and OCP. The experiment halted when the current density rose to 1.5 mA·cm^{-2}. Each specimen at different temperatures was tested 3–5 times.

The EIS was employed to probe the properties of the passive film. The solution was maintained at a constant temperature of 85 °C. The test frequency range spanned 100 kHz–0.01 Hz. Sinusoidal potentials, ranging from 10 mV (vs. OCP) to 0.20 V (vs. SCE), were applied. Notably, in a 1 M NaCl solution at 85 °C, the OCP values for 2205-A and 2205-B were measured at -0.203 ± 0.028 V (vs. SCE) and -0.219 ± 0.071 V (vs. SCE), respectively. The real part, imaginary part, and phase angle of the interface between specimen surface and solution were recorded at different test frequencies. Lastly, data fitting was performed using ZView software.

The PPT was utilized for pitting control. Following a constant 85 °C cathodic polarization and OCP in 1 M NaCl solution, a high potential (E_h) of 0.85 V was applied for 10 s, followed by a low potential (E_l) of 0 V for 50 s. This cycle of high and low potentials was repeated 100 times, and the current curve was recorded over time.

Potentiostatic polarization (PSP) experiments were conducted to investigate the metastable pitting of 2205 DSS. After cathodic polarization and OCP, the specimen was immersed in 1 M NaCl solution at 50 °C and a constant potential of 200 mV (vs. SCE) was applied for 1200 s. The data acquisition rate in these experiments was approximately 100 Hz.

Characterization

An optical microscope (OM; ZEISS Axiocam 208) was employed to examine surface pitting after PPT. Quantitative analysis was subsequently conducted using OM stitching techniques. The pit size after PPT was measured by a confocal laser scanning microscopy (CLSM; ZEISS LSM900). The duplex microstructure of the 2205 DSS was revealed through etching via immersion in Murakami's reagent (30 g KOH, 30 g potassium ferricyanide, 100 mL water) at 90 °C for 30 s. The austenite (γ) appeared white and ferrite (α) brown. If carbides were present, they were etched to appear black[83].

X-ray diffraction (XRD; Rigaku Ultimate IV) analysis were carried out on the surface of the 2205 DSS using a Rigaku Ultimate IV powder X-ray diffractometer, equipped with Cu K$_\alpha$ radiation.

Scanning electron microscopy (SEM; ZEISS GeminiSEM 300) equipped with energy-dispersed spectroscopy (EDS; Oxford Xplore) was used to examine the morphology and composition of the inclusions. The localized Volta potential of the inclusions within the specimens was characterized using an atomic force microscope (AFM; Bruker) in combination with scanning Kelvin probe force microscopy (SKPFM) under atmospheric conditions.

Data availability

The relevant data are available from the corresponding author upon reasonable request.

References

1. Frankel, G. S., Li, T. & Scully, J. R. Perspective—localized corrosion: passive film breakdown vs pit growth stability. *J. Electrochem. Soc.* **164**, C180–C181 (2017).
2. Frankel, G. S. & Sridhar, N. Understanding localized corrosion. *Mater. Today* **11**, 38–44 (2008).
3. Sun, L. et al. Point defect model for passivity breakdown on hyperduplex stainless steel 2707 in solutions containing bromide at different temperatures. *Corros. Sci.* **194**, 109959 (2022).
4. Sun, L. et al. Mixed potential model for passivity characters of hyperduplex stainless steel 2707 in ammonium carbonate solution containing chloride. *Corros. Sci.* **201**, 110302 (2022).
5. Deng, B. et al. Application of the modified electrochemical potentiodynamic reactivation method to detect susceptibility to intergranular corrosion of a newly developed lean duplex stainless steel LDX2101. *Corros. Sci.* **52**, 969–977 (2010).
6. Deng, B. et al. Effect of thermal cycles on the corrosion and mechanical properties of UNS S31803 duplex stainless steel. *Corros. Sci.* **51**, 2969–2975 (2009).
7. Tan, H. et al. Annealing temperature effect on the pitting corrosion resistance of plasma arc welded joints of duplex stainless steel UNS S32304 in 1.0 M NaCl. *Corros. Sci.* **53**, 2191–2200 (2011).
8. Tan, H. et al. Influence of welding thermal cycles on microstructure and pitting corrosion resistance of 2304 duplex stainless steels. *Corros. Sci.* **55**, 368–377 (2012).
9. Sun, Y., Tan, X., Lei, L., Li, J. & Jiang, Y. Revisiting the effect of molybdenum on pitting resistance of stainless steels. *Tungsten* **3**, 329–337 (2021).
10. Han, Y. et al. A short review on the role of alloying elements in duplex stainless steels. *Tungsten* https://doi.org/10.1007/s42864-022-00168-z (2022).
11. Muthupandi, V., Bala Srinivasan, P., Seshadri, S. K. & Sundaresan, S. Effect of weld metal chemistry and heat input on the structure and properties of duplex stainless steel welds. *Mater. Sci. Eng: A* **358**, 9–16 (2003).

12. Dong, H. et al. Effect of aging time on electrochemical corrosion behavior of 2101 duplex stainless steel. *Acta Metall. Sin* **45**, 919–923 (2009).

13. Tang, Y., Dai, N., Wu, J., Jiang, Y. & Li, J. Effect of surface roughness on pitting corrosion of 2205 duplex stainless steel investigated by electrochemical noise measurements. *Materials* **12**, 738 (2019).

14. Lei, L. et al. Understanding the pitting mechanism of super ferritic stainless steel in bromide solutions: the role of Ti/Nb–Mo precipitates with a core–shell structure. *Corros. Sci.* **199**, 110176 (2022).

15. Tan, X. et al. Roles of different components of complex inclusion in pitting of 321 stainless steel: Induction effect of CaS and inhibition effect of TiN. *Corros. Sci.* **209**, 110692 (2022).

16. Wang, R. Precipitation of sigma phase in duplex stainless steel and recent development on its detection by electrochemical potentiokinetic reactivation: a review. *Corros. Commun.* **2**, 41–54 (2021).

17. Ma, L., Wiame, F., Maurice, V. & Marcus, P. Origin of nanoscale heterogeneity in the surface oxide film protecting stainless steel against corrosion. *Npj Mater. Degrad.* **3**, 1–9 (2019).

18. Ma, L., Lynch, B., Wiame, F., Maurice, V. & Marcus, P. Nanoscale early oxidation mechanisms of model FeCrNi austenitic stainless steel surfaces at room temperature. *Corros. Sci.* **190**, 109653 (2021).

19. Li, T., Scully, J. R. & Frankel, G. S. Localized corrosion: passive film breakdown vs pit growth stability: Part II. A model for critical pitting temperature. *J. Electrochem. Soc.* **165**, C484–C491 (2018).

20. Li, T., Scully, J. R. & Frankel, G. S. Localized corrosion: passive film breakdown vs pit growth stability: Part V. validation of a new framework for pit growth stability using one-dimensional artificial pit electrodes. *J. Electrochem. Soc.* **166**, C3341–C3354 (2019).

21. Li, T., Scully, J. R. & Frankel, G. S. Localized corrosion: passive film breakdown vs. pit growth stability: Part IV. The role of salt film in pit growth: a mathematical framework. *J. Electrochem. Soc.* **166**, C115–C124 (2019).

22. Li, T., Wu, J. & Frankel, G. S. Localized corrosion: passive film breakdown vs. Pit growth stability, Part VI: Pit dissolution kinetics of different alloys and a model for pitting and repassivation potentials. *Corros. Sci.* **182**, 109277 (2021).

23. Sun, Y., Wang, J., Jiang, Y. & Li, J. A comparative study on potentiodynamic and potentiostatic critical pitting temperature of austenitic stainless steels. *Mater. Corros.* **69**, 44–52 (2018).

24. Erazmus-Vignal, P., Vignal, V., Saedlou, S. & Krajcarz, F. Corrosion behaviour of sites containing (Cr, Fe)2N particles in thermally aged duplex stainless steel studied using capillary techniques, atomic force microscopy and potentiostatic pulse testing method. *Corros. Sci.* **99**, 194–204 (2015).

25. Vignal, V., Richoux, V., Suzon, E., Thiébaut, S. & Tabaleiv, K. The use of potentiostatic pulse testing to study the corrosion behavior of welded stainless steels in sodium chloride solution. *Mater. Des.* **88**, 186–195 (2015).

26. Zhang, Z., Han, D., Jiang, Y., Shi, C. & Li, J. Microstructural evolution and pitting resistance of annealed lean duplex stainless steel UNS S32304. *Nucl. Eng. Des.* **243**, 56–62 (2012).

27. Murkute, P., Pasebani, S., & Burkan Isgor, O. Metallurgical and electrochemical properties of super duplex stainless steel clads on low carbon steel substrate produced with laser powder bed fusion. *Sci. Rep.* **10**, 10162 (2020).

28. Guo, Y. et al. Microstructure evolution and pitting corrosion resistance of the Gleeble-simulated heat-affected zone of a newly developed lean duplex stainless steel 2002. *J. Alloy. Compd.* **658**, 1031–1040 (2016).

29. Boissy, C., Ter-Ovanessian, B., Mary, N. & Normand, B. Correlation between predictive and descriptive models to characterize the passive film – Study of pure chromium by electrochemical impedance spectroscopy. *Electrochim. Acta* **174**, 430–437 (2015).

30. Cui, Z. et al. Passivation behavior and surface chemistry of 2507 super duplex stainless steel in acidified artificial seawater Containing Thiosulfate. *J. Electrochem. Soc.* **164**, C856 (2017).

31. Duan, Z. et al. Pitting behavior of SLM 316L stainless steel exposed to chloride environments with different aggressiveness: pitting mechanism induced by gas pores. *Corros. Sci.* **167**, 108520 (2020).

32. Hirschorn, B. et al. Constant-phase-element behavior caused by resistivity distributions in films: II. Applications. *J. Electrochem. Soc.* **157**, C458 (2010).

33. Córdoba-Torres, P. et al. On the intrinsic coupling between constant-phase element parameters α and Q in electrochemical impedance spectroscopy. *Electrochim. Acta* **72**, 172–178 (2012).

34. Pahlavan, S. et al. Pitting corrosion of martensitic stainless steel in halide bearing solutions. *Corros. Sci.* **112**, 233–240 (2016).

35. Peguet, L., Gaugain, A., Dussart, C., Malki, B. & Baroux, B. Statistical study of the critical pitting temperature of 22-05 duplex stainless steel. *Corros. Sci.* **60**, 280–283 (2012).

36. Chen, B. et al. Use of the potentiostatic pulse technique to study and influence pitting behavior of 317L stainless steel. *J. Electrochem. Soc.* **167**, 041509 (2020).

37. Pistorius, P. C. & Burstein, G. T. Metastable pitting corrosion of stainless steel and the transition to stability. Philosophical Transactions of the Royal Society of London. *Series A: Phys. Eng. Sci.* **341**, 531–559 (1997).

38. Frankel, G. S., Stockert, L., Hunkeler, F. & Boehni, H. Metastable pitting of stainless steel. *Corrosion* **43**, 429–436 (1987).

39. Abbasi Aghuy, A., Zakeri, M., Moayed, M. H. & Mazinani, M. Effect of grain size on pitting corrosion of 304L austenitic stainless steel. *Corros. Sci.* **94**, 368–376 (2015).

40. Pahlavan, S., Moayed, M. H., Kosari, A. & Mirjalili, M. Investigation of the microstructure dependence of critical pitting temperature and pitting potential in a 2205 duplex stainless steel. *J. Electrochem. Soc.* **168**, 111501 (2021).

41. Sun, D. M., Jiang, Y. M. & Tang, Y. Pitting corrosion behavior of stainless steel in ultrasonic cell. *Electrochim. Acta* **54**, 1558–1563 (2009).

42. Ghahari, M. et al. Synchrotron X-ray radiography studies of pitting corrosion of stainless steel: extraction of pit propagation parameters. *Corros. Sci.* **100**, 23–35 (2015).

43. Srinivasan, J., McGrath, M. J. & Kelly, R. G. A high-throughput artificial pit technique to measure kinetic parameters for pitting stability. *J. Electrochem. Soc.* **162**, C725 (2015).

44. Srinivasan, J., Liu, C. & Kelly, R. G. Geometric evolution of flux from a corroding one-dimensional pit and its implications on the evaluation of kinetic parameters for pit stability. *J. Electrochem. Soc.* **163**, C694 (2016).

45. Li, T., Liu, L., Zhang, B., Li, Y. & Wang, F. Growth kinetics of metastable pits on sputtered nanocrystalline stainless steel. *Corros. Sci.* **124**, 46–55 (2017).

46. Almuaili, F. A., McDonald, S. A., Withers, P. J., Cook, A. B. & Engelberg, D. L. Strain-induced reactivation of corrosion pits in austenitic stainless steel. *Corros. Sci.* **125**, 12–19 (2017).

47. Galvele, J. R. Transport Processes and the mechanism of pitting of metals. *J. Electrochem. Soc.* **123**, 464 (1976).

48. Yang, Y., Hou, X.-L. & Li, M.-C. Effect of vacuum pressure on the initiation and propagation of pitting corrosion of 2205 duplex stainless steel in concentrated seawater. *Acta Metall. Sin. Engl. Lett.* **35**, 1023–1033 (2022).

49. Shang, B. et al. Effects of grain boundary characteristics changing with cold rolling deformation on intergranular corrosion resistance of 443 ultra-pure ferritic stainless steel. *Corros. Commun.* **8**, 27–39 (2022).

50. Gao, J., Jiang, Y., Deng, B., Ge, Z. & Li, J. Determination of pitting initiation of duplex stainless steel using potentiostatic pulse technique. *Electrochim. Acta* **55**, 4837–4844 (2010).

51. Sathirachinda, N., Pettersson, R. & Pan, J. Depletion effects at phase boundaries in 2205 duplex stainless steel characterized with SKPFM and TEM/EDS. *Corros. Sci.* **51**, 1850–1860 (2009).

52. Zheng, S., Li, C., Qi, Y., Chen, L. & Chen, C. Mechanism of (Mg,Al,Ca)-oxide inclusion-induced pitting corrosion in 316L stainless steel exposed to sulphur environments containing chloride ion. *Corros. Sci.* **67**, 20–31 (2013).

53. Liu, C. et al. Towards a better understanding of localised corrosion induced by typical non-metallic inclusions in low-alloy steels. *Corros. Sci.* **179**, 109150 (2021).

54. Liu, C. et al. New insights into the mechanism of localised corrosion induced by TiN-containing inclusions in high strength low alloy steel. *J. Mater. Sci. Technol.* **124**, 141–149 (2022).

55. Kim, S. Y., Kwon, H. S. & Kim, H. S. Effect of delta ferrite on corrosion resistance of type 316L stainless steel in acidic chloride solution by micro-droplet cell. *Solid State Phenom.* **124–126**, 1533–1536 (2007).

56. Otake, A., Muto, I., Chiba, A., Sugawara, Y. & Hara, N. Pitting at the δ/γ boundary of Type 304 stainless steel in NaCl solution: the role of oxide inclusions and segregation. *J. Electrochem. Soc.* **164**, C991–C1002 (2017).

57. Zhang, H., Li, C., Yao, G. & Zhang, Y. Effect of inclusion interface evolution on the thermal stability of cellular substructures in additively manufactured stainless steel. *Mater. Sci. Eng.* **841**, 143045 (2022).

58. Sun, Y. et al. Mechanisms of inclusion-induced pitting of stainless steels: a review. *J. Mater. Sci. Technol.* **168**, 143–156 (2024).

59. Suito, H. & Inoue, R. Thermodynamics on control of inclusions composition in ultraclean steels. *ISIJ Int.* **36**, 528–536 (1996).

60. Shibata, H., Tanaka, T., Kimura, K. & Kitamura, S.-Y. Composition change in oxide inclusions of stainless steel by heat treatment. *Ironmak. Steelmak.* **37**, 522–528 (2010).

61. Shibata, H., Kimura, K., Tanaka, T. & Kitamura, S. Mechanism of change in chemical composition of oxide inclusions in Fe–Cr alloys deoxidized with Mn and Si by heat treatment at 1473 K. *ISIJ Int.* **51**, 1944–1950 (2011).

62. Kong, D. et al. Heat treatment effect on the microstructure and corrosion behavior of 316L stainless steel fabricated by selective laser melting for proton exchange membrane fuel cells. *Electrochim. Acta* **276**, 293–303 (2018).

63. Tokuda, S., Muto, I., Sugawara, Y. & Hara, N. High-temperature heat-treatment at 1673 K: improvement of pitting corrosion resistance at inclusions of type 304 stainless steel under applied stress. *Mater. Trans.* **63**, 265–268 (2022).

64. Liu, J., Wu, H., Bao, Y. & Wang, M. Inclusion variations and calcium treatment optimization in pipeline steel production. *Int. J. Min. Mat.* **18**, 527–534 (2011).

65. Muto, I., Ito, D. & Hara, N. Microelectrochemical investigation on pit initiation at sulfide and oxide inclusions in Type 304 stainless steel. *J. Electrochem. Soc.* **156**, C55 (2009).

66. Sathirachinda, N., Pettersson, R., Wessman, S. & Pan, J. Study of nobility of chromium nitrides in isothermally aged duplex stainless steels by using SKPFM and SEM/EDS. *Corros. Sci.* **52**, 179–186 (2010).

67. Revilla, R. I., Liang, J., Godet, S. & De Graeve, I. Local corrosion behavior of additive manufactured AlSiMg alloy assessed by SEM and SKPFM. *J. Electrochem. Soc.* **164**, C27–C35 (2017).

68. Liu, C. et al. Effect of inclusions modified by rare earth elements (Ce, La) on localized marine corrosion in Q460NH weathering steel. *Corros. Sci.* **129**, 82–90 (2017).

69. Liu, C. et al. Role of Al2O3 inclusions on the localized corrosion of Q460NH weathering steel in marine environment. *Corros. Sci.* **138**, 96–104 (2018).

70. Liu, C. et al. Influence of rare earth metals on mechanisms of localised corrosion induced by inclusions in Zr-Ti deoxidised low alloy steel. *Corros. Sci.* **166**, 108463 (2020).

71. Man, C., Dong, C., Xiao, K., Yu, Q. & Li, X. The combined effect of chemical and structural factors on pitting corrosion induced by MnS-(Cr, Mn, Al)O duplex inclusions. *Corrosion* **74**, 312–325 (2018).

72. Liu, C., Zhang, L., Ren, Y. & Zhang, J. Review on effect of non-metallic inclusions on pitting corrosion resistance of stainless steel. *J. Iron Steel Res.* **33**, 1040–1051 (2021).

73. Park, J. H. & Kang, Y. Inclusions in stainless steels − a review. *Steel Res. Int.* **88**, 1700130 (2017).

74. Guo, X. et al. Self-accelerated corrosion of nuclear waste forms at material interfaces. *Nat. Mater.* **19**, 310–316 (2020).

75. Galvele, J. R. Transport processes and the mechanism of pitting of metals. *J. Electrochem. Soc.* **123**, 464–474 (1976).

76. Galvele, J. Transport processes in passivity breakdown—ii. Full hydrolysis of the metal ions. *Corros. Sci.* **21**, 551–579 (1981).

77. Kovalov, D., Taylor, C. D., Heinrich, H. & Kelly, R. G. Operando electrochemical TEM, ex-situ SEM and atomistic modeling studies of MnS dissolution and its role in triggering pitting corrosion in 304L stainless steel. *Corros. Sci.* **199**, 110184 (2022).

78. Krawiec, H., Vignal, V., Heintz, O. & Oltra, R. Influence of the chemical dissolution of MnS inclusions on the electrochemical behavior of stainless steels. *Electrochem. Soc.* **152**, 213–219 (2005).

79. Chiba, A., Muto, I., Sugawara, Y. & Hara, N. A microelectrochemical system for in situ high-resolution optical microscopy: morphological characteristics of pitting at MnS inclusion in stainless steel. *J. Electrochem. Soc.* **159**, C341–C350 (2012).

80. Chiba, A. et al. Microelectrochemical aspects of interstitial carbon in type 304 stainless steel: improving pitting resistance at MnS inclusion. *J. Electrochem. Soc.* **162**, C270–C278 (2015).

81. Chiba, A., Muto, I., Sugawara, Y. & Hara, N. Effect of atmospheric aging on dissolution of MnS inclusions and pitting initiation process in type 304 stainless steel. *Corros. Sci.* **106**, 25–34 (2016).

82. Shimahashi, N., Muto, I., Sugawara, Y. & Hara, N. Effects of corrosion and cracking of sulfide inclusions on pit initiation in stainless steel. *J. Electrochem. Soc.* **161**, C494–C500 (2014).

83. Inoue, H. & Koseki, T. Solidification mechanism of austenitic stainless steels solidified with primary ferrite. *Acta Mater.* **124**, 430–436 (2017).

Acknowledgements

Author contributions
Guoyong Ran: Conceptualization, Investigation, Writing. Wenrui Tu: Analysis of electrochemical data. Haopeng Dong: Data analysis. Yiming Jiang: Funding acquisition, Supervision. Jin Li: Supervision. Kezhao Liu: Funding acquisition. Yangting Sun: Conceptualization, Writing, Funding acquisition.

Competing interests
The authors declare no competing interests.

Additional information
Correspondence and requests for materials should be addressed to Yangting Sun.

Reprints and permissions information is available at http://www.nature.com/reprints